

Comparing the first- and second-order theories of relativistic dissipative fluid dynamics using the $1+1$ dimensional relativistic flux corrected transport algorithm

Etele Molnár^a

Frankfurt Institute for Advanced Studies, Johann Wolfgang Goethe Universität, Max-von-Laue-Str. 1, 60438 Frankfurt am Main, Germany

Received: 20 July 2008 / Revised: 22 December 2008 / Published online: 24 February 2009

© Springer-Verlag / Società Italiana di Fisica 2009

Abstract Focusing on the numerical aspects and accuracy we study a class of bulk viscosity driven expansion scenarios using the relativistic Navier–Stokes and truncated Israel–Stewart form of the equations of relativistic dissipative fluids in $1+1$ dimensions. The numerical calculations of conservation and transport equations are performed using the numerical framework of flux corrected transport. We show that the results of the Israel–Stewart causal fluid dynamics are numerically much more stable and smoother than the results of the standard relativistic Navier–Stokes equations.

PACS 25.75.-q · 24.10.Nz

1 Introduction

The recent discovery of near perfect fluidity of hot QCD matter at the Relativistic Heavy Ion Collider (RHIC) [1] brought about a lot of attention for and interest in modeling the collective phenomena in relativistic heavy-ion collisions using the relativistic dissipative fluid dynamical approach. In contrast to perfect fluid dynamical models, dissipative fluids provide a more accurate and physically more plausible description incorporating first- and second-order corrections compared to perfect fluids.

These higher-order corrections are irreversible; thermal conductivity and dissipation are related to temperature gradients and inhomogeneities of the flow field. A linear relation between the two establishes transport equations, where the parameters entering these equations are the so-called transport coefficients: for thermal conductivity λ , shear viscosity η , and bulk viscosity ζ , also referred to as second viscosity or volume viscosity [2–6].

Recently many studies have specifically investigated the fluid dynamical description of matter created at RHIC including shear viscosity; see [7–17] and references therein. Some of these calculations [10, 13] made use of the first-order theory by Eckart [2], and Landau and Lifshitz [3], but the main focus was on the second-order causal theory of dissipative fluid dynamics by Israel and Stewart [4–6], and the theory by Öttinger and Grmela [18].

These calculations particularly examined the effect of a small shear viscosity motivated by the conjectured lower bound from the AdS/CFT correspondence [19–21]. It was found only recently that, contrary to perturbative QCD estimates [22], lattice QCD reveals a large increase of the bulk viscosity near the critical temperature [23–25]. This numerical evidence motivates studies of the evolution of matter with large viscosity. It has also been suggested that a large bulk viscosity near T_c may entirely change the standard picture of adiabatic hadronization employed so far in hydrodynamical models [26, 60].

In this paper we address the phenomena related to viscous evolution of matter in $1+1$ dimensional systems neglecting the contribution of heat conduction. We focus on the numerical implementation of both the first-order and second-order approaches and investigate specific test cases to clarify numerical aspects and accuracy of the solutions. This represents an important first step before multi-dimensional models can be constructed and applied. We also show how the relaxation equations for the dissipative corrections in the second-order theory can be solved efficiently and accurately also via the flux corrected transport algorithm by writing them in the form of continuity equations with a source.

The paper is organized as follows. First, we briefly recapitulate and formulate the equations of dissipative fluid dynamics and the numerical method which will be used to

^a e-mail: molnar@fias.uni-frankfurt.de

solve the respective equations. Afterwards we present and discuss the results in several cases. To our knowledge major parts of this work, including the specific comparisons between the first-order and second-order theories, are presented and discussed in detail for the first time.

2 The equations of dissipative fluid dynamics

We adopt the standard notation for four-vectors and tensors and use the natural units, $\hbar = c = k = 1$, throughout this paper. The upper Greek indices denote contravariant while the lower indices denote covariant objects. The Roman indices or bold faced letters denote three-vectors.

In the Eckart frame, the conserved charge four-current is $N^\mu = nu^\mu$, where n is the local rest frame conserved charge density, $u^\mu = (\gamma, \gamma \mathbf{v})$ is the four-flow of matter normalized to one, $u^\mu u_\mu = 1$, and the relativistic gamma is $\gamma = 1/\sqrt{1 - \mathbf{v}^2}$. The dissipative energy-momentum tensor is $T^{\mu\nu} = (e + \Pi)u^\mu u^\nu - (p + \Pi)g^{\mu\nu} + \pi^{\mu\nu}$, where $e = u_\mu T^{\mu\nu} u^\nu$ is the local rest frame energy density, the orthogonal projection of the energy-momentum tensor, $p(e, n) + \Pi = -\frac{1}{3}\Delta_{\mu\nu} T^{\mu\nu}$ denotes the local equilibrium pressure plus the bulk pressure and $g^{\mu\nu} \equiv g_{\mu\nu} = \text{diag}(1, -1, -1, -1)$ is the metric of the flat space-time. The stress tensor, $\pi^{\mu\nu} = [\frac{1}{2}(\Delta_\alpha^\mu \Delta_\beta^\nu + \Delta_\alpha^\nu \Delta_\beta^\mu) - \frac{1}{3}\Delta^{\mu\nu} \Delta_{\alpha\beta}]T^{\alpha\beta}$, is the symmetric, traceless quantity $\pi^{\mu\nu} g_{\mu\nu} = 0$, and we write the part of the energy-momentum tensor orthogonal to the flow velocity $\pi^{\mu\nu} u_\nu = 0$. The local conservation of charge, energy, and momentum requires that

$$\partial_\mu N^\mu = 0, \quad (2.1)$$

$$\partial_\mu T^{\mu\nu} = 0, \quad (2.2)$$

and the second law of thermodynamics demands that the four-divergence of the entropy four-current is non-decreasing and positive,

$$\partial_\mu S^\mu \geq 0. \quad (2.3)$$

Here $\partial_\mu = (\partial_t, \partial_i)$ denotes the four-divergence, where $\partial_t \equiv \partial/\partial t$ is the time derivative and $\partial_i \equiv \partial/\partial x_i = (\partial/\partial x, \partial/\partial y, \partial/\partial z)$ is the divergence operator.

The explicit form of the conservation equations for charge, energy, and momentum are

$$\partial_t N^0 + \partial_i N^i = 0, \quad (2.4)$$

$$\partial_t T^{00} + \partial_i T^{0i} = 0, \quad (2.5)$$

$$\partial_t T^{0j} + \partial_i T^{ij} = 0, \quad (2.6)$$

where we defined the conserved charge density N^0 , the charge flux N^i , the total energy density T^{00} , the energy flux density T^{0i} , the momentum flux density T^{ij} and the

momentum flux density tensor T^{ij} . These laboratory frame quantities can be expressed in terms of the local rest frame quantities and velocity by

$$N^0 \equiv n\gamma, \quad (2.7)$$

$$N^i \equiv n\gamma v_i, \quad (2.8)$$

$$T^{00} \equiv (e + p + \Pi)\gamma^2 - (p + \Pi) + \pi^{00}, \quad (2.9)$$

$$\begin{aligned} T^{0i} &\equiv (e + p + \Pi)\gamma^2 v_i + \pi^{0i}, \\ &= v_i T^{00} + v_i(p + \Pi) - v_i\pi^{00} + \pi^{0i}, \end{aligned} \quad (2.10)$$

$$\begin{aligned} T^{ij} &\equiv (e + p + \Pi)\gamma^2 v_i v_j - (p + \Pi)g^{ij} + \pi^{ij}, \\ &= v_i T^{0j} - (p + \Pi)g^{ij} - v_i\pi^{0j} + \pi^{ij}. \end{aligned} \quad (2.11)$$

The relation between the local rest frame and laboratory frame quantities can be calculated using the above equations; hence

$$n = N^0 \sqrt{1 - v^2}, \quad (2.12)$$

$$e = (T^{00} - \pi^{00}) - v_i(T^{0i} - \pi^{0i}), \quad (2.13)$$

where the absolute value of the velocity is $v \equiv |\mathbf{v}|$. These local rest frame quantities are needed to calculate the pressure, $p(e, n)$, from the equation of state (EOS).

The fluid velocity and relativistic gamma can be calculated from (2.10), therefore

$$v_i = \frac{(T^{0i} - \pi^{0i})}{(T^{00} - \pi^{00}) + P(e, n, \Pi)}, \quad (2.14)$$

$$\gamma = \frac{1}{\sqrt{1 - v^2}}, \quad (2.15)$$

where $P(e, n, \Pi) = p(e, n) + \Pi$ gives the correction to the equilibrium pressure absorbed in the trace of the energy-momentum tensor.

2.1 1 + 1 dimensional expansion

For simple 1 + 1 dimensional systems in 1 + 3 dimensional space-time, where $u^\mu = \gamma(1, 0, 0, v_z)$, the equations of dissipative fluid dynamics reduce to a similar form as in the case of perfect fluids. Let us denote the pressure in the longitudinal direction by $P_z \equiv p + \Pi + \pi = P(e, n, \Pi) + \pi$, where $\pi = \pi^{zz}/\gamma^2$ is the local rest frame value of the stress. By construction, the tracelessness property implies that $\pi^{xx} = \pi^{yy} = -\pi/2$ and $\pi^{00} = v_z^2 \gamma^2 \pi$. The orthogonality relations will further reduce the number of unknowns; note that $\pi^{0x} = \pi^{0y} = 0$, $\pi^{0z} \equiv v_z \pi^{zz} = v_z \gamma^2 \pi$, and all non-diagonal components of the stress tensor vanish, $\pi_{i \neq j}^{ij} = 0$, thus the only component of the shear tensor we have to propagate is π [27].

The conservation equations follow from (2.4, 2.5, 2.6),

$$\partial_t N^0 + \partial_z (v_z N^0) = 0, \quad (2.16)$$

$$\partial_t T^{00} + \partial_z (v_z T^{00}) = -\partial_z (v_z P_z), \quad (2.17)$$

$$\partial_t T^{0z} + \partial_z (v_z T^{0z}) = -\partial_z P_z, \quad (2.18)$$

where the laboratory frame quantities are

$$N^0 = n\gamma, \quad (2.19)$$

$$T^{00} = (e + P_z)\gamma^2 - P_z, \quad (2.20)$$

$$T^{0z} = (e + P_z)\gamma^2 v_z. \quad (2.21)$$

The local rest frame variables expressed through the laboratory frame quantities, the velocity and relativistic gamma are

$$n = N^0 \sqrt{1 - v_z^2}, \quad (2.22)$$

$$e = T^{00} - v_z T^{0z}, \quad (2.23)$$

$$v_z = \frac{T^{0z}}{T^{00} + P_z}, \quad (2.24)$$

$$\gamma = \frac{1}{\sqrt{1 - v_z^2}}, \quad (2.25)$$

while the local rest frame effective pressure is

$$P_z = p(e, n) + \Pi + \pi. \quad (2.26)$$

Here the equilibrium pressure is given by the equation of state, $p = c_s^2 e$, where c_s is the local speed of sound. The equations and quantities for a perfect fluid are obtained in the limit of vanishing dissipation, corresponding to $P_z \rightarrow p(e, n)$, while the form of conservation equations and the expressions relating the laboratory frame quantities to the rest frame quantities and the calculation of the velocity are formally the same as for perfect fluids.

The last two variables that remain to be explicitly defined are the bulk pressure and the shear. These can be calculated from (2.1, 2.2, 2.3) using different approaches. To study the various methods is out of the scope of the current manuscript; however, these theories and recent new phenomenological developments aimed to extend the theory of dissipative fluids shed light on the open questions related to the ambiguities on this matter; see for example [28–38] and references therein.

In the first-order theories of Eckart [2] or Landau and Lifshitz [3], i.e., the relativistic Navier–Stokes equations, the entropy four-current is decomposed as $S^\mu = su^\mu + \beta q^\mu$, where q^μ is the heat flux, s is the local rest frame entropy density and $\beta = 1/T$ is the inverse temperature. These last two scalar quantities satisfy the fundamental relation of thermodynamics, $s = \beta(e + p)$, for matter with no conserved

charge. Hence, in first-order theories the only way to satisfy the second law of thermodynamics, using a linear relationship between the thermodynamic force and flux, is to choose

$$\pi_{\text{NS}} \equiv \pi = -\frac{4}{3}\eta\theta, \quad (2.27)$$

$$\Pi_{\text{NS}} \equiv \Pi = -\zeta\theta, \quad (2.28)$$

where η and ζ are positive coefficients of shear and bulk viscosity respectively, while $\theta \equiv \partial_\mu u^\mu$ is the expansion scalar. The first-order theories (contrary to second-order theories) are known to have intrinsic problems attributed to the immediate appearance and disappearance of the thermodynamic flux once the thermodynamic force is turned on or off. As shown by Hiscock and Lindblom [39–42] the linearized version of these equations propagate perturbations acausally, and even though initially these might be weak signals they may grow unbounded bringing the system out of stable equilibrium.

To remedy some of these problems the second-order theory of Israel and Stewart was constructed [4–6], similarly to the non-relativistic theory by Müller [43]. This was built around the assumption that the entropy four-current contains second-order corrections in dissipation due to viscosity (here we disregard heat conductivity and cross couplings) such that $S^\mu = su^\mu + \beta q^\mu - (\beta/2)(\beta_0 \Pi^2 + 3\beta_2 \pi^2/2)u^\mu$, where β_0 and β_2 are thermodynamic coefficients related to the relaxation times. Applying the law of positive entropy production and some algebra leads to the transport equations for the shear and bulk pressure,

$$u^\mu \partial_\mu \pi = \frac{1}{\tau_\pi} (\pi_{\text{NS}} - \pi), \quad (2.29)$$

$$u^\mu \partial_\mu \Pi = \frac{1}{\tau_\Pi} (\Pi_{\text{NS}} - \Pi), \quad (2.30)$$

where the relaxation time of bulk viscosity and shear are $\tau_\pi = 2\eta\beta_2$ and $\tau_\Pi = \zeta\beta_0$. The above equations are referred as the truncated Israel–Stewart equations, since terms involving the divergence of the flow field and thermodynamic coefficients have been neglected compared to the equations by Israel and Stewart [11]. However, the current form of the transport equations already captures the essential features of relaxation phenomena which make the theory causal and stable.

Another crucial difference between first- and second-order theories is in the mathematical structure of the equations. In first-order theories the viscous corrections appear linearly proportional to the divergence of the flow field, therefore they are more sensitive to fluctuations and the inhomogeneities in the flow field; see Sect. 4. In second-order theory not only the coefficients of viscosity but also the thermodynamic coefficients need to be specified. For example the latter parameters are known for a relativistic Boltzmann

gas of massive particles [4–6], $\beta_0 = 216(m\beta)^{-4}/p$, leading to a relaxation time of $\tau_\Pi = 216(m\beta)^{-4}(\zeta/p)$, which is divergent for a fluid of massless particles, while the bulk viscosity coefficient is zero in that limit. The thermodynamic coefficient for the shear viscosity within the same substance is $\beta_2 = 3/(4p)$, leading to the relaxation time of, $\tau_\pi = (3/2)(\eta/p)$.

In passing we point out a few important facts regarding the bulk viscosity and its source. For a long time in the classical non-relativistic Navier–Stokes theory the purpose of bulk viscosity was controversial [44]. Even Eckart in his pioneering work [2] was concerned with fluids without bulk viscosity. Israel was the first to show that the bulk viscosity of relativistic matter may not be unimportant [45]. This turned the attention mainly in cosmology, rendering bulk viscosity as the only possible form of dissipative phenomena; see for example [46, 47] and references therein for a thorough introduction. The bulk viscous effects are important in mixtures when the difference in properties between the components becomes substantial. This might be due to the difference in cooling rates within the same type of substance or in a mixture between massive and effectively massless particles during a phase transition [48] (for other possible sources for bulk viscosity, see [49]). Therefore in these situations bulk viscosity is used to describe a mixture effectively as a single fluid with a non-vanishing bulk viscosity coefficient and relaxation time.

It is also important to phenomenologically understand the relation between viscosity and relaxation time [3]. For example, bulk or volume viscosity appears when the system undergoes an isotropic expansion or contraction. If this happens at a relatively fast rate such that the system is unable to follow the change in volume and restore equilibrium in a short time, then this means that the relaxation time of the viscous pressure is long. On the opposite, if the system equilibrates almost immediately, then the corresponding relaxation time must be short. Hence it is also intuitive that large deviations from equilibrium can only be the consequence of a large viscosity, while small departures from equilibrium result from small viscosity, assuming in both cases that the expansion rate is considerably small. It is also fundamental that the relaxation time must be shorter than the inverse of the expansion rate of the system, $\tau_{\pi,\Pi} \ll 1/\theta$; otherwise the system will never be able to equilibrate and the fluid dynamical approach is unsuitable.

In case of a relativistic Boltzmann gas, recalling the viscosity coefficients from (2.27, 2.28), we find that the relaxation times are

$$\tau_\pi = -\frac{d_\pi}{\theta} \left(\frac{\pi_{\text{NS}}}{p_{\text{eq}}} \right), \quad (2.31)$$

$$\tau_\Pi = -\frac{d_\Pi}{\theta} \left(\frac{\Pi_{\text{NS}}}{p_{\text{eq}}} \right), \quad (2.32)$$

where $d_\pi = 9/8$ and we can only assume, similarly to the relaxation time for the shear, that d_Π is a dimensionless positive number on the order of unity. This also follows from the fact that both viscosities give birth to a local dissipative pressure, which for small dissipative corrections relax to the Navier–Stokes values. In case the dissipative pressure is comparable to the equilibrium pressure, the relaxation times become longer than the mean free time between collisions; thus the fluid dynamical approach may no longer be appropriate.

3 The numerical scheme

Here we briefly review the basic principles of the underlying numerical scheme used in this work. The explicit finite difference scheme called sharp and smooth transport algorithm (SHASTA) [50, 51] is a version of the flux corrected transport (FCT) algorithm. Detailed tests, simulations and comparisons to semi-analytical solutions have been performed with this algorithm in various situations; in non-relativistic and relativistic perfect fluid dynamics and magnetohydrodynamics, in the last decades [52–56] achieving confidence and wide usage.

Before discussing the version of the algorithm in detail, let us rewrite the conservation equations (2.16, 2.17, 2.18) and transport equations (2.29, 2.30) in conservation form, which makes it possible to treat all equations with the same numerical scheme. Due to similarity in form and effect in case of 1 + 1 dimensional expansion scenarios, we include only one type of viscosity and relaxation equation and refer to it as bulk viscosity in the following. Hence,

$$\partial_t R + \partial_z (v_z R) = 0, \quad (3.1)$$

$$\partial_t E + \partial_z (v_z E) = -\partial_z (v_z P_z), \quad (3.2)$$

$$\partial_t M_z + \partial_z (v_z M_z) = -\partial_z P_z, \quad (3.3)$$

where $R = N^0$, $E = T^{00}$, $M_z = T^{0z}$, and $P_z = p + \pi$ or $P_z = p + \Pi$. Introducing a common notation, $\tilde{\Phi} = \gamma\Phi$, for the auxiliary variables, $\tilde{\pi} = \gamma\pi$ and/or $\tilde{\Pi} = \gamma\Pi$, the relaxation equations (2.29, 2.30) can be rewritten¹ in a form similar to the conservation equations,

$$\partial_t \tilde{\Phi} + \partial_z (v_z \tilde{\Phi}) = \frac{1}{\tau_\Phi} (\Phi_{\text{NS}} - \Phi) + \theta \Phi, \quad (3.4)$$

where Φ , Φ_{NS} and τ_Φ commonly denote the shear pressure and its relaxation time and/or the bulk viscous pressure and its relaxation time.

¹Another possibility would be to rewrite the relaxation equation as, $\partial_t \Phi + \partial_z (v_z \Phi) = \frac{1}{\gamma \tau_\Phi} (\Phi_{\text{NS}} - \Phi) + (\partial_z v_z) \Phi$.

The above conservation and transport equations are of conservation type, written generally as

$$\partial_t U + \partial_z (vU) = S(t, z), \quad (3.5)$$

where $U = U(t, z)$ is one of the conserved quantities, $v = v_z$ is the velocity, and $S(t, z)$ is the source term. The discretized conservative variable defined as an average in cell, j , at coordinate point, z_j , at discrete time level, t^n , is denoted by U_j^n . Some of the source terms in our examples contain differential operations, therefore they are represented as finite (second-order) central differences, i.e., for spatial derivatives $\Delta S_j = (S_{j+1}^n - S_{j-1}^n)/2\Delta z$.

In the SHASTA algorithm the velocity, the local rest frame variables and source terms, are computed and updated at half time steps, i.e., in $\Delta t/2$ time intervals. This requirement ensures second-order accuracy in both space and time. In contrast, the conservative variables, U , used to advance the solution from time level n to $n+1$, are updated only once at the end of full time steps. In a given cell, j , this can be summarized formally as

$$U^{n+1/2} \sim \tilde{U}^n(U^n, v^n, S^n), \quad (3.6)$$

$$U^{n+1} \sim \tilde{U}^n(U^n, v^{n+1/2}, S^{n+1/2}). \quad (3.7)$$

In case of the relaxation equation, the source terms contain dynamical information on the divergence of the flow field in both space and time. Second-order accuracy in time can only be calculated in Δt time intervals (if we use the time-split method), at time levels, $n - 1/2, n, n + 1/2, n + 1, \dots$, where the time derivatives are $\Delta S^n \sim (S^n - S^{n-1})/\Delta t$, $\Delta S^{n+1/2} \sim (S^{n+1/2} - S^{n-1/2})/\Delta t$, etc. This ensures better accuracy (however, the difference is rather small) than on calculating the time derivatives as well as the source terms at full time steps only, i.e., only between time levels n and $n + 1$.

The difference of primary variables in adjacent cells is denoted by $\Delta_j \equiv U_{j+1}^n - U_j^n$ or later also by $\tilde{\Delta}_j = \tilde{U}_{j+1} - \tilde{U}_j$. The explicit SHASTA method [50, 51] at half step as well as at full step first computes the so-called transported and diffused quantities,

$$\begin{aligned} \tilde{U}_j &= \frac{1}{2} (Q_+^2 \Delta_j - Q_-^2 \Delta_{j-1}) \\ &+ (Q_+ - Q_-) U_j^n + \Delta t \Delta S, \end{aligned} \quad (3.8)$$

where

$$Q_{\pm} = \frac{1/2 \mp \epsilon_j}{1 \pm (\epsilon_{j\pm1} - \epsilon_j)}, \quad (3.9)$$

$$\epsilon_j = \lambda v_j^{n+1/2}, \quad (3.10)$$

and the Courant number is the ratio of time step to cell size, $\lambda = \Delta t / \Delta z$. A general requirement for any finite differ-

ence algorithm is to fulfill the so-called Courant–Friedrichs–Lewy (CLF) criterion, i.e., $\lambda \leq 1$, related to the stability of hyperbolic equations; otherwise the numerical solution becomes unconditionally unstable. Physically this expresses that matter must be causally propagated at most $\Delta z = \Delta t$ to distance into vacuum. For SHASTA, $\lambda \leq 1/2$, while in this paper we use a smaller value, $\lambda = 0.4$. Here we note that since the numerical algorithms average the transported quantities over a cell, part of the matter is acausally propagated over $(1 - \lambda)\Delta z$. This is a purely numerical artifact called prediffusion.

The time-advanced quantities are calculated removing the numerical diffusion by subtracting the so-called antidiiffusion fluxes, \tilde{A} , from the transported and diffused quantities such that

$$U_j^{n+1} = \tilde{U}_j - \tilde{A}_j + \tilde{A}_{j-1}. \quad (3.11)$$

Here we have defined the flux corrected antidiiffusion flux

$$\tilde{A}_j = \sigma_j \min[0, \max(\sigma_j \tilde{\Delta}_{j+1}, |A_j|, \sigma_j \tilde{\Delta}_{j-1})], \quad (3.12)$$

where the ‘phoenical’ antidiiffusion flux² is

$$A_j = \frac{A_{\text{ad}}}{8} \left[\tilde{\Delta}_j - \frac{1}{8} (\Delta_{j+1} - 2\Delta_j + \Delta_{j-1}) \right], \quad (3.13)$$

$$\sigma_j = \text{sgn}(A_j). \quad (3.14)$$

The so-called mask, A_{ad} , is introduced to regulate the amount of antidiiffusion [57]. The algorithm tends to produce small wiggles, due to the fact that in the antidiiffusion step one removes too much diffusion; therefore, adjusting the mask, one can suppress this artifact leading to a more stable and smoother solutions. However, the drawback is that by reducing the antidiiffusion we increase the numerical diffusion causing larger prediffusion and entropy production even in perfect fluids! This step is unavoidable in numerical algorithms in which due to discretization the differential equations are truncated already at leading order, and without additional but with purely numerical corrections they lead to unstable solutions. Within the numerical framework this is called numerical dissipation, or, since it acts similarly to the physical viscosity, it is also called artificial or numerical viscosity [58].

In case we want to model physical viscosity one has to keep in mind that there is already a small numerical viscosity in the algorithm, which has to be estimated (for example, by measuring the entropy production in case of a perfect fluid) and taken into account. This leads to a total effective viscosity which is larger than the one we explicitly

²The explicit antidiiffusion flux [50, 51], $A_j = A_{\text{ad}} \tilde{\Delta}_j / 8$, leads to somewhat smoother results.

include. Obviously, things are not as simple, since the numerical viscosity and numerical diffusion contain linear and non-linear parts [56], and its effect strongly depends on the grid size, initial condition and flux limiters we use. Therefore, it is a question of numerical analysis and extensive testing to reveal the effect of numerical viscosity. Some can be found in the original or related publications of the numerical schemes.

It is important to remember that SHASTA is a low implicit viscosity algorithm, and it conserves energy (and momentum) up to 5 digits, but produces entropy in the case of a perfect fluid roughly between 0.5% and 5%, depending on the initial setup, antidiffusion flux, mask coefficient and physical situation. The lower value was found in the studies we are going to show in the next section, using a mask of $A_{ad} = 0.8$, while the error is less than 0.2% using the standard value, $A_{ad} = 1$, after 200 time steps. The large entropy production was found in the case of a 3D grid with the same proportions, cell size, number of time steps and reduced mask coefficient in case of 1 + 3 dimensional expansion into vacuum of an initially constant energy sphere.

To determine the bulk viscous pressure one also has to calculate the expansion scalar, $\theta(t, z)$. One possibility is to take the standard form, used in this work, using a second-order accurate central difference formula, $\theta \equiv \partial_t \gamma + \partial_z(v_z \gamma) = \gamma^3(v_z \partial_t v_z + \partial_z v_z)$. The other form can be expressed from the conservation of energy, $u_\nu \partial_\mu T^{\mu\nu} = 0$, or in case we also have conserved charge, from the continuity equation, $\partial_\mu N^\mu = 0$, leading to $\theta = -\gamma(\partial_t e + v_z \partial_z e)/(e + p + \Pi + \pi) = -\gamma(\partial_t n + v_z \partial_z n)/n$.

The numerical differentiation of the velocity field introduces obvious numerical problems, which we need to address. In particular, finite differences of the velocity field in adjacent cells, usually fluctuate due to numerical noise. Since we solve a set of non-linear coupled partial differential equations, these may become uncontrollable. To make the numerical expansion rate smoother we found that an additional five-point stencil smoothing is necessary.³ However, the maximum number of neighboring cells to include is restricted by the Courant number; otherwise we acausally propagate information into the neighboring cells. In our example the maximal number of these cells are two to the right and two to the left, hence the five-point stencil.

In the first- and second-order theories the dissipative pressure must be smaller than the equilibrium pressure, $|\Pi| \leq p_{eq}$. If the correction to the equilibrium pressure is small, the system will continue to expand with a lower effective pressure, but the overall behavior should not change

³In a loose sense this coarse-graining of the expansion rate may be viewed as providing a “mass” to fluctuations with wavelength on the order of the grid spacing.

considerably from the perfect fluid limit. However, at different parts of the system the local expansion rate may become very large (for example, in the transition region to vacuum) and generate large dissipative corrections. This threshold is given by the equilibrium pressure locally, at least in the first-order theory. Hence, even though the physical situation may encounter larger values of the bulk pressure, we choose to keep this maximum. The upper bound imposed on the bulk pressure leads to an upper bound for the local expansion rate, $\theta_{max} = p_{eq}/\zeta$. In other words, the Navier–Stokes bulk pressure is defined to be $\Pi_{NS} = -\zeta\theta$ for $\theta < \theta_{max}$ and $\Pi_{NS}^{max} = -\zeta\theta_{max}$ for $\theta \geq \theta_{max}$. In the latter region the total pressure vanishes and the acceleration therefore stalls.

We keep the above convention also for second-order theory, so that for very short relaxation times we exactly approach the Navier–Stokes limit. It is also important to mention that, since we solve the relaxation equation in conservation form, the expansion rate appears explicitly in the truncated equations as well, similarly as in the full Israel–Stewart equations. Hence it is obviously necessary to find an upper bound for terms containing the expansion rate; otherwise those terms may grow unbounded and destabilize the solutions.

4 Results and discussion

In all numerical calculations, we have fixed the following parameters. The Courant number is $\lambda = 0.4$, and the cell size is $dz = 0.2$ fm; therefore $dt = 0.08$ fm/c. The grid contains 240 cells, while the total number of time steps is $n = 200$, which corresponds to $\Delta t = 16$ fm/c expansion time. The amount of antidiffusion is reduced by 20%, i.e., $A_{ad} = 0.8$, which leads to some prediffusion but returns smoother profiles. The thermodynamic quantities are given by the Stefan–Boltzmann relations where the degeneracy of massless particles is $g = 16$. In case of dissipative fluids, the bulk viscosity coefficient to entropy density ratio is constant, with values corresponding to small, $\zeta/s = 0.2$, and to large, $\zeta/s = 1$, ratios.

In most situations the initial expansion rate is unknown; therefore the dissipative corrections are neglected at start. This may only last for one time step, since after that the time derivatives can already be calculated and dissipative corrections added. In particular cases, such as the Bjorken scaling solution, the expansion rate can be inferred from the geometry; therefore it does not pose a problem. We will return to this issue in Sect. 4.5.

The relaxation time is given similarly to (2.32); therefore $\tau_\Pi = -\frac{1}{\theta}(\frac{\Pi_{NS}}{p_{eq}})$. We have checked the asymptotic limits of the relaxation equations. In case the relaxation time is small, $\tau_\Pi \approx dt$, the effect of bulk viscosity is immediately felt by the system, and therefore the system behaves as in the case

of first-order theories. For very large relaxation times, i.e., larger than the lifetime of the system, and small initial dissipation, the effect of viscosity is exponentially suppressed and the solution approaches the perfect fluid limit.

4.1 Expansion into vacuum of perfect fluid

In case of perfect fluids one of the analytical solutions which relates the thermodynamic properties of matter and the type of fluid dynamical solution is the $1+1$ dimensional expansion into vacuum. This is a special case of the relativistic Riemann problem describing 1-dimensional time-dependent flow. The initial conditions are such that initially at $t=0$ half of the space, $z \leq 0$, is filled uniformly with fluid at rest, $v(z, 0) = 0$, with energy density $e(z, 0) = e_0$, while the positive half $z > 0$ is (empty) filled with vacuum.

One can show that for thermodynamically normal matter, e.g., a massless ideal gas with the EOS, $p(e) = c_s^2 e$, where $c_s^2 = 1/3$ is the speed of sound squared, the stable solution to the fluid dynamical equations is a simple rarefaction wave. The rarefaction wave is a wave for which the energy density decreases in the direction of propagation, but the profile of the flow does not change with time as a function of the similarity variable,

$$\xi \equiv \frac{z}{t} = \frac{v(e) - c_s}{1 - v(e)c_s}. \quad (4.1)$$

Here we recall the analytic results for a perfect fluid in the forward light-cone [53]. The energy density as a function of the similarity variable for $-1 \leq \xi \leq -c_s$ is constant,

$$e(\xi) = c_s^{-2} p_0, \quad (4.2)$$

while in the region $-c_s \leq \xi \leq 1$ the matter starts to rarefy and the energy density decreases as

$$e(\xi) = c_s^{-2} p_0 \left(\frac{1 - c_s}{1 + c_s} \frac{1 - \xi}{1 + \xi} \right)^{(1+c_s^2)/(2c_s)}. \quad (4.3)$$

The temperature can be inferred from standard thermodynamical relations and the EOS, leading to

$$T(\xi) = T_0 \left(\frac{e(\xi)}{e_0} \right)^{c_s^2/(1+c_s^2)}. \quad (4.4)$$

We also compare how well the fluid flow is reproduced by the numerical calculation, where the analytical solution as a function of energy density is

$$v(e) = \frac{1 - (e/e_0)^{2c_s/(1+c_s^2)}}{1 + (e/e_0)^{2c_s/(1+c_s^2)}}. \quad (4.5)$$

The velocity can be given as a function of the similarity variable as well from (4.1). This is plotted in Fig. 4.1a. The

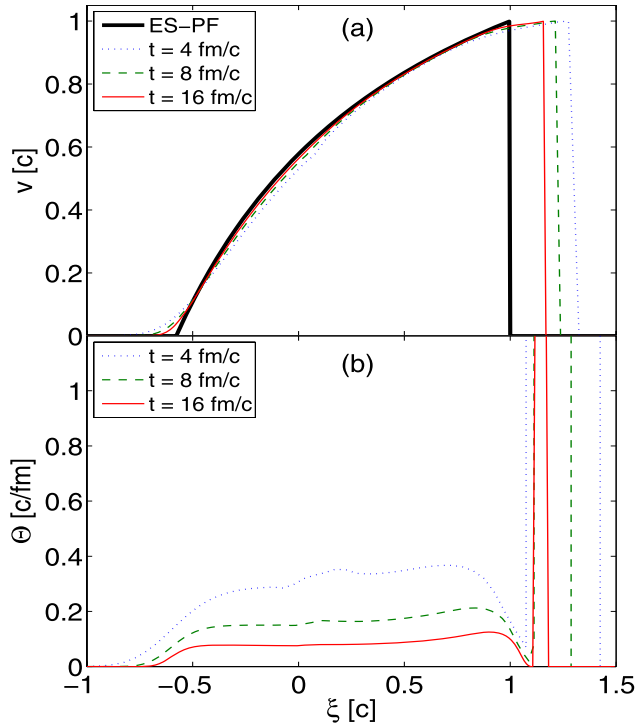


Fig. 4.1 The exact solution in case of a perfect fluid (thick line) and numerical solutions (thin dotted line at $t = 4$ fm/c, thin dashed line at $t = 8$ fm/c, and thin line at $t = 16$ fm/c) as a function of the similarity variable $\xi(z, t)$. **a** The flow velocity $v(\xi)$; **b** the expansion scalar $\theta(\xi)$

results for the expansion scalar calculated numerically are shown in Fig. 4.1b.

Figure 4.2a shows the temperature normalized by the initial temperature, from (4.4), while Fig. 4.2b, shows the lab frame energy density normalized by the initial pressure as a function of the similarity variable. The thick line shows the exact solution for a perfect fluid (ES-PF), while the numerical solutions also for a perfect fluid are at $t = 4$ fm/c with a thin dotted line, at $t = 8$ fm/c with a thin dashed line, and at $t = 16$ fm/c with a full thin line.

Both figures compare the analytical solutions to the numerical solutions, to pinpoint how well the underlying numerical method reproduces the ES-PF. We see that the numerical solutions asymptotically approach the exact result, while they also reduce the numerical prediffusion into vacuum. This is due to the fact that the initially sharp discontinuity smears out as the rarefaction wave covers an increasing number of cells. Due to prediffusion and coarse-graining, the expansion rate is not zero for $\xi > 1$, as can be seen in both figures; this problem mostly affects the acausally propagated low density matter. For a perfect fluid the numerical results are smooth and very nicely reproduce (especially at later times) the exact results. The larger deviations from the ES-PF around the boundary to vacuum is due to a somewhat large prediffusion caused by the reduced antidiiffusion, while the deviations around $-c_s$ are due to a larger numer-

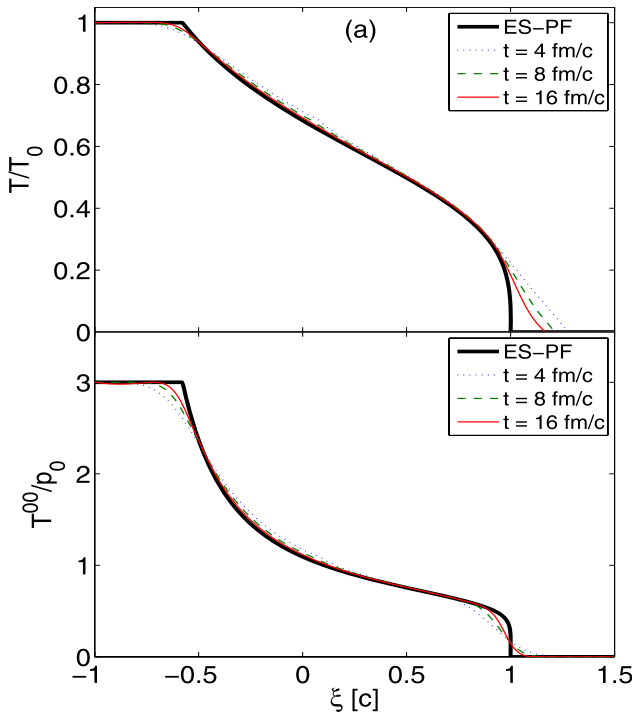


Fig. 4.2 **a** The temperature normalized to the initial temperature, $T(\xi)/T_0$; **b** the laboratory frame energy density normalized to the initial pressure $T^{00}(\xi)/\rho_0$; both as a function of the similarity variable $\xi(z, t)$. The parameters are the same as in Fig. 4.1

ical diffusion. A more thorough study of the expansion into vacuum of a perfect fluid can be found in Ref. [53].

4.2 Expansion into vacuum with small and large dissipation

Here we analyze and study the behavior of dissipative fluids corresponding to the first-order and second-order theories, and we plot the numerical results next to the exact solution in case of a perfect fluid. In all figures, unless stated otherwise, all quantities are plotted as a function of the similarity variable; the ES-PF is plotted with a dotted line, while the numerical solutions at $t = 4 \text{ fm}/c$ appear with a thin dashed line and at $t = 16 \text{ fm}/c$ with a continuous line. The upper bound for the bulk pressure is $\Pi^{\max} \equiv p_{\text{eq}}$, and the relaxation time is $\tau_{\Pi} = -\frac{1}{\theta}(\frac{\Pi_{\text{NS}}}{p_{\text{eq}}}) \text{ fm}/c$. The ratio of viscosity over entropy density corresponds to small $\zeta/s = 0.2$ or large $\zeta/s = 1.0$ values.

Figure 4.3a shows the velocity profile calculated from first-order theory, while Fig. 4.3b comes from second-order theory. We see that for first-order theory the velocity is fluctuating with an increasing frequency in time. Initially the amplitude and the wavelength of the fluctuations is large; however as the expansion proceeds these large fluctuations are damped and become smaller amplitude and smaller wavelength oscillations. This is partially due to the initial

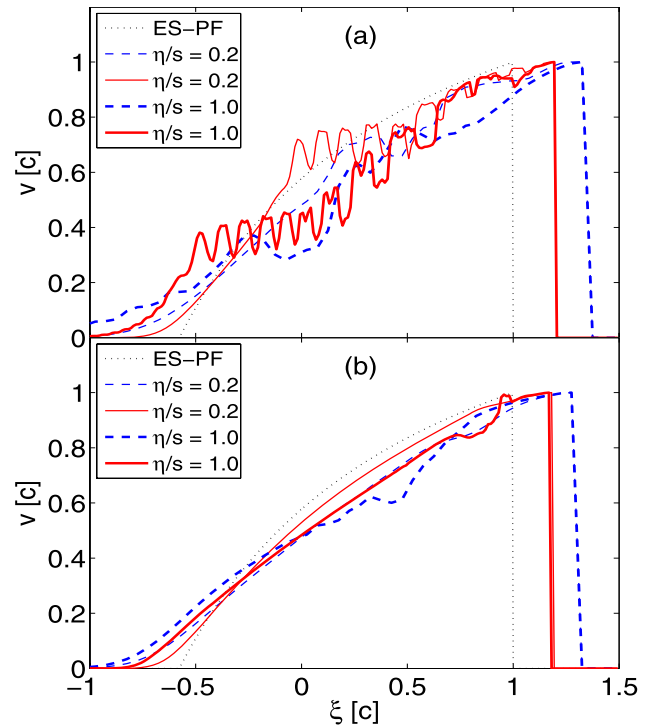


Fig. 4.3 The velocity profile for a perfect fluid ES-PF compared to dissipative fluids with $\zeta/s = 0.2$ (thin) and $\zeta/s = 1.0$ (thick), as numerically calculated and plotted at $t = 4 \text{ fm}/c$ (dashed) and $t = 16 \text{ fm}/c$ (full); **a** first-order theory; **b** second-order theory

discontinuity being smeared out in time and the problem is resolved on a larger grid. However, the damping is also due to the non-linear antidiiffusion term (3.12) in the numerical algorithm. In other words this is numerical viscosity, which always acts to smooth the fluxes, contrary to the numerical dispersion, which acts exactly in the opposite direction and produces ripples in the results. It should also be obvious that working on a larger grid with the same cell size would not improve the results!

For bigger viscosity, the numerical fluctuations become larger, which is clearly a sign that the method fails and the numerical errors become uncontrollable. The results for second-order theory are much smoother and show that there is a relevant change in the velocity profile, which is an outcome of the large dissipative pressure. This interesting phenomenon appears near the edge of the matter, where due to a large bulk pressure contribution the effective pressure essentially vanishes; therefore, that part of the system stops to accelerate. But due to inertia it keeps moving forward with constant speed, hence forming a constant velocity plateau. Note that the small wiggle in the velocity profile for large dissipation, visible for example on Fig. 4.3b, is an artifact of the phoenical antidiiffusion flux.

Figures 4.4a and b shows the expansion scalar calculated numerically at different time steps for both theories. We can see that in the case of first-order theory, the expansion scalar

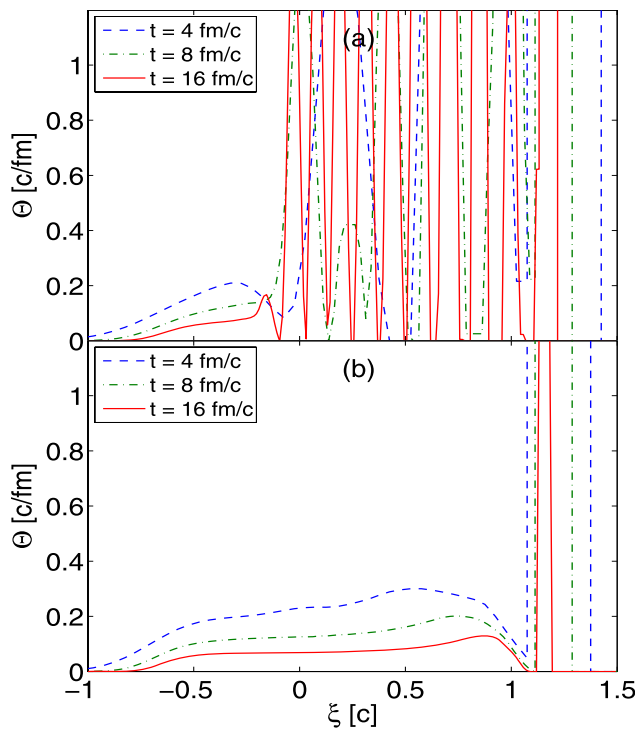


Fig. 4.4 The calculation of the expansion scalar at different time steps in the case of a dissipative fluid with $\xi/s = 0.2$. **a** First-order theory; **b** second-order theory

is highly fluctuating, while in second-order theory it is much smoother. Both calculations reflect the space-time inhomogeneity of the flow field amplified by the velocity.

For a better understanding, we have plotted the effective pressure as a function of the similarity variable in Fig. 4.5 for both theories. One can see that for early times the expansion rate, and therefore the bulk viscous pressure, is largest. When the effective pressure drops (to zero), the acceleration of matter is reduced (the matter flows with constant velocity). However, the expansion rate will also decrease later, reducing the viscous pressure; and therefore the velocity will continue to increase. The important thing to remember is that the speed of sound decreases due to dissipation and the effective rarefaction speed [59] can be given as $c_{\text{eff}}^2 \sim (p + \Pi)/e$.

It is also interesting to remark that even though the bulk viscosity is large at places, the effective pressure (and therefore the equilibrium pressure) may be larger than in the case of perfect fluid, due to the fact that the thermodynamic state of the system is influenced by entropy production and slower cooling. This is why the lab frame energy density decreases more slowly; see Fig. 4.7.

Figure 4.6 shows the temperature profile plotted at different time steps for both theories. As in the case of velocity, the presence of viscosity is observable in the overall reduced cooling of matter. The increase in the expansion rate increases the dissipation which in turn slows the expansion,

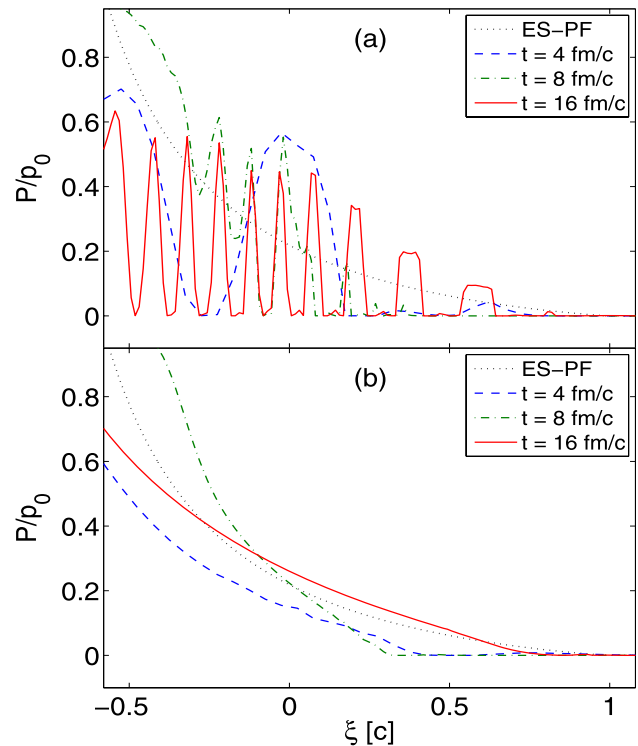


Fig. 4.5 The effective pressure normalized by the initial pressure with dissipation proportional to $\xi/s = 1$. **a** First-order theory; **b** second-order theory

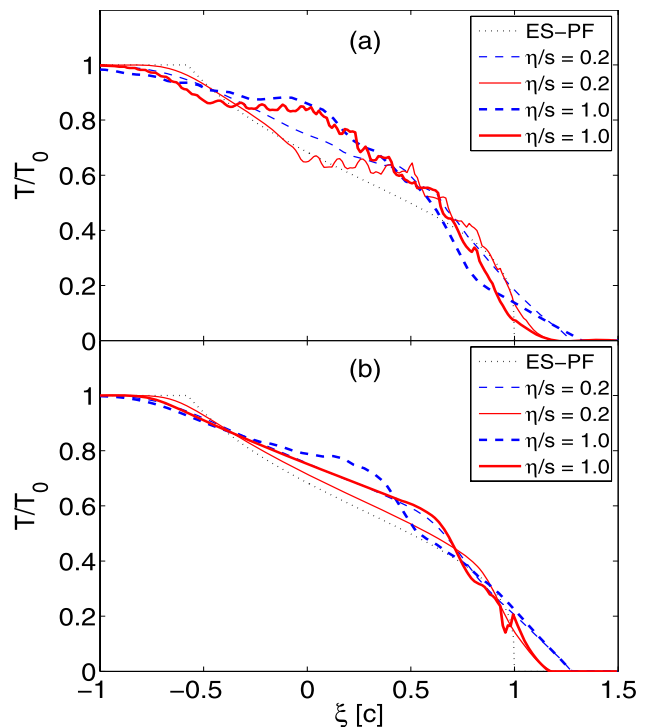


Fig. 4.6 The temperature normalized by the initial temperature. **a** First-order theory; **b** second-order theory. The parameters are the same as in Fig. 4.3

thus the matter cools at a slower rate. On the other hand in first-order theories, the visibility of this effect is much more reduced due to numerical problems.

The laboratory frame energy density normalized to the initial pressure is presented in Fig. 4.7. Since this quantity is proportional to the fourth root of the temperature divided by the initial temperature, it is much less affected by the fluctuations and prediffusion in both cases. Based on the previous arguments the deviation from the ES-PF are noticeable for larger values of the similarity variable, where the effect of dissipation is most pronounced. This plot also confirms that the effective pressure drops to zero; however, since the matter has a finite energy density, temperature, and velocity, the laboratory energy density is not zero at those places. As soon as the expansion rate decreases, the finite albeit small effective pressure will continue to expand the matter into vacuum. Further comparisons between the first-order and second-order theories can be found in the appendix.

4.3 Expansion into vacuum with a soft EOS

To further investigate the behavior of matter with large viscosity we have used a relatively soft EOS, where the speed of sound squared is $c_s^2 = 1/15$, while keeping the other parameters intact. Using a soft equation of state reduces the pressure and the pressure gradients in the system, while the re-

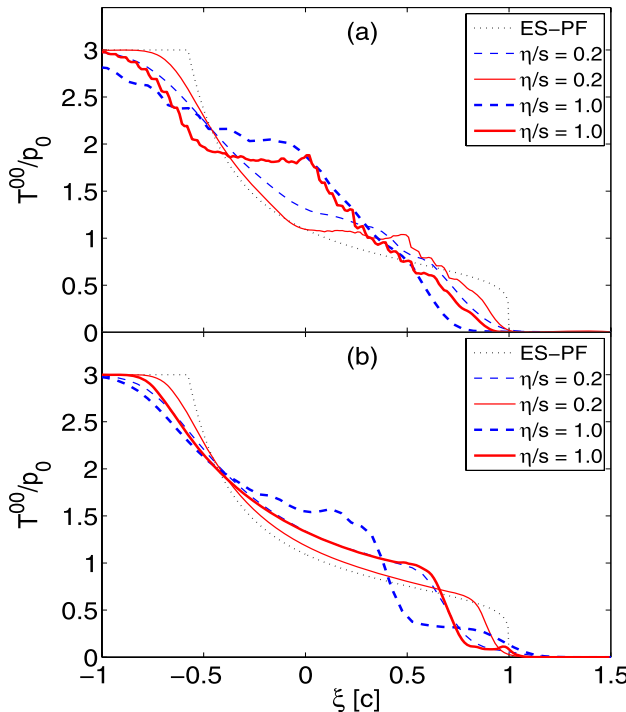


Fig. 4.7 The laboratory frame energy density normalized to the initial pressure. **a** First-order theory; **b** second-order theory. The parameters are the same as in Fig. 4.3

laxation time increases, inversely with local speed of sound and temperature, $\tau_{\Pi} \sim (1 + c_s^2)/(c_s^2 T)$.

Figure 4.8a shows the velocity profile for first-order theory while Fig. 4.8b for second-order theory, both in case of a soft EOS. In comparison to Fig. 4.3, the velocity profiles are much improved and the constant velocity part of velocity profile is clearly visible even from the first-order theory. It is clear that the algorithm works much better, producing overall smooth results. We have also checked our algorithm with a hard EOS, $e = p$, which proved that overshoots and oscillations become enhanced compared to the standard case ($c_s^2 = 1/3$) and the results became less reliable.

Figure 4.9 shows the effective pressure normalized by the initial pressure, similar to Fig. 4.5, but with a soft EOS. Once again the results are good, especially in the case of second-order theory. This is due to fact that a softer EOS not only reduces the thermodynamic pressure compared to the standard EOS but also decreases the dissipative pressure. It is also important to understand that in this case the dissipative effects act on an overall wider scale as function of ξ , but even though the effect of dissipation is immediately added, the results are much smoother because the dissipative pressure is also reduced.

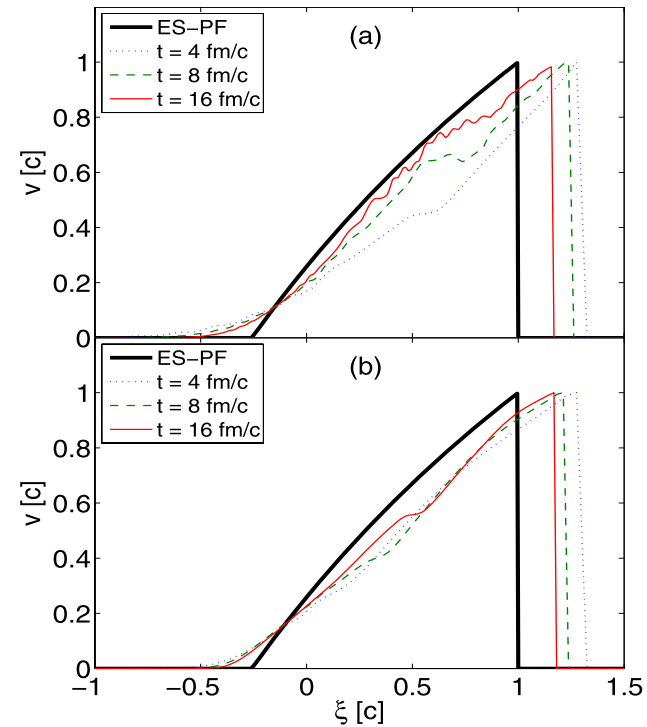


Fig. 4.8 The velocity profile for a perfect fluid (ES-PF), compared to a dissipative fluid with $\zeta/s = 1$, using a soft EOS. **a** First-order theory; **b** second-order theory

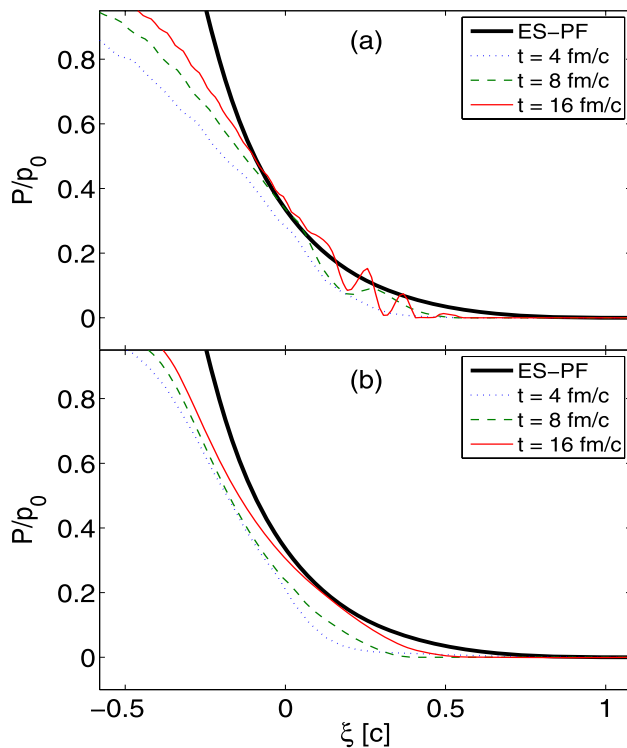


Fig. 4.9 The effective pressure normalized by the initial pressure for a soft EOS. **a** First-order theory; **b** second-order theory

4.4 Expansion into vacuum of a matter with temperature-dependent bulk viscosity

An interesting and relevant question to study is the expansion of dissipative matter with a temperature-dependent bulk viscosity. To model this property, we assumed that bulk viscosity acts in the close vicinity of a specific or critical temperature, $T = T_c(1 \pm 0.02)$, and otherwise it is zero. Thus the bulk viscosity coefficient is

$$\zeta = \zeta_0 \Theta(T - 1.02T_c)(1 - \Theta(T - 0.98T_c)). \quad (4.6)$$

Here the choice of critical temperature is $T_c = 2T_0/3$, where T_0 is the initial temperature, and $\zeta_0 = s$ is the bulk viscosity coefficient. The calculations are done for second-order theory including the above temperature-dependent bulk viscosity.

Figures 4.10a and b shows the velocity of the matter and the expansion rate as a function of the similarity variable. For the same setup, in Figs. 4.11a and b the temperature normalized by the initial temperature and the laboratory frame energy density normalized by the initial pressure is shown.

When the temperature falls in the respective regime, the viscosity over entropy ratio rises suddenly, to $\zeta_0/s = 1$, while otherwise the dissipation is switched off. In our case this manifests itself as almost constant velocity temperature, pressure, and energy density plateau, located roughly

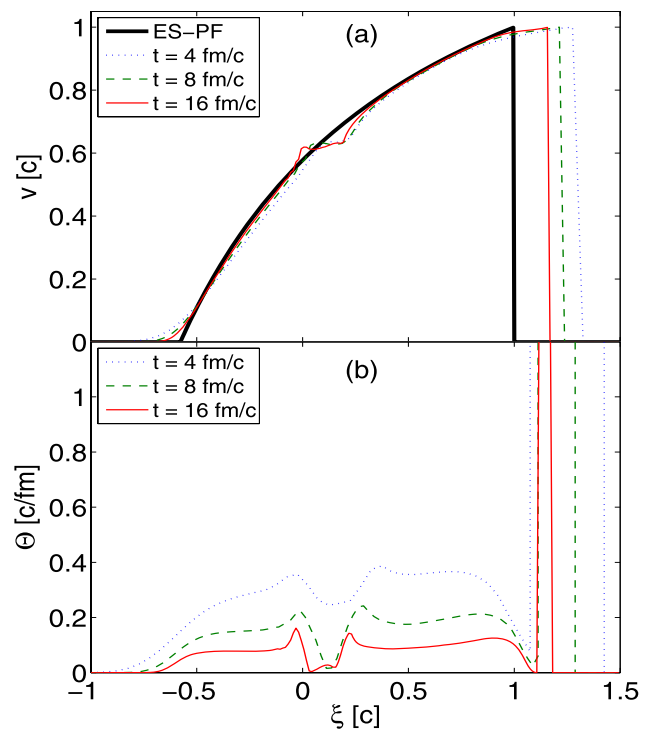


Fig. 4.10 The velocity profile **a**, and the numerical calculation of the expansion scalar **b**, using a temperature-dependent bulk viscosity for second-order theory

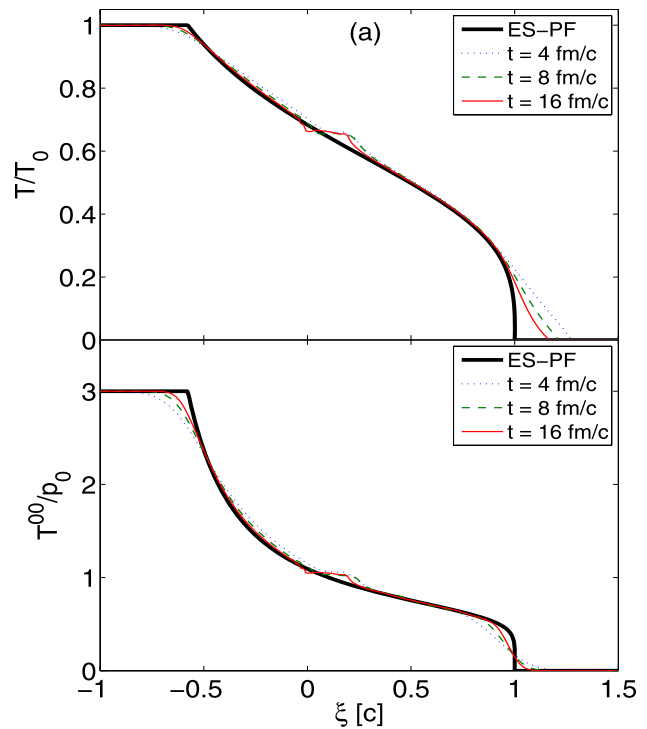


Fig. 4.11 The parameters are the same as in Fig. 4.10. **a** The temperature normalized to the initial temperature, $T(\xi)/T_0$; **b** the laboratory frame energy density normalized to the initial pressure $T^{00}(\xi)/p_0$

between $0 < \xi < 0.2$. Because the effective pressure decreased suddenly, the matter is slowed down considerably, until the matter cools below the predefined temperature (although much slower); then the system will suddenly find local thermal equilibrium and continue to accelerate. This is apparent in all plots. This type of studies may be relevant in case of a phase transition where the temperature-dependent viscosity modeling becomes necessary [60].

4.5 The Bjorken solutions for perfect and dissipative fluids

In this section we test how well the numerical calculations reproduce 1-dimensional dissipative scaling flow. The relaxation time was kept constant, $\tau_\Pi = 1 \text{ fm}/c$, which does not effect the final outcome qualitatively.

We first recall the $1 + 1$ dimensional Bjorken scaling solution for perfect [61] and dissipative fluids [7, 8]. The equations follow from the conservation law, $\partial_\mu T^{\mu\nu} = 0$, and the second law of thermodynamics, under the assumption that the matter expands longitudinally with a flow velocity $v = z/t$ in a boost-invariant manner. To transform the partial differential equations into simple differential equations (using the assumption of boost invariance), one carries out a coordinate transformation from (t, z) to (τ, η) , where $\tau = \sqrt{t^2 - z^2}$ is the proper time and $\eta = \frac{1}{2} \log[(t+z)/(t-z)]$ is the space-time rapidity. Therefore, the truncated Israel–Stewart equations for the energy and bulk pressure are

$$\frac{de}{d\tau} = -\frac{1}{\tau}(e + p + \Pi), \quad (4.7)$$

$$\frac{d\Pi}{d\tau} = \frac{1}{\tau_\pi}(\Pi_{\text{NS}} - \Pi), \quad (4.8)$$

where $\Pi_{\text{NS}} = -\zeta/\tau$, and the effective pressure satisfies $d(p + \Pi)/d\eta = 0$. The equations of perfect fluid dynamics are obtained when the dissipative bulk pressure is zero, $\Pi(\tau) = 0$. The relativistic Navier–Stokes equation is given by (4.7) alone, since the bulk pressure, $\Pi(\tau) = \Pi_{\text{NS}}(\tau)$, is given algebraically.

In the Bjorken picture the system is infinitely elongated in rapidity. Since our SHASTA code is written in standard space-time coordinates (t, z) , we have to determine initial values on a $t = t_0$ surface and the fluid must have a finite length (due to the finite grid), $-z_0 \leq z \leq z_0$. This is done as follows.

We first solve (4.7, 4.8) using a fourth-order Runge–Kutta solver for all times $\tau \geq \tau_0 = 1 \text{ fm}/c$. Together with the assumption of boost invariance, this determines the hydrodynamic fields in the entire forward light cone. We then repeat the solution with the SHASTA partial differential equation solver with initial conditions at $t_0 = z_0 + \Delta z = 6 \text{ fm}$ set by the Runge–Kutta solution. We note that in the SHASTA solution the system has a boundary, since the velocity at z_0

is close to but slightly less than the velocity of light (z_0 is smaller than t_0 by one grid spacing).

In the first-order theory the initial value for the bulk pressure is $\Pi_{\text{NS}} = -\zeta_0/\tau_0$, which can be limited by the equilibrium pressure, i.e., the dissipative pressure should not be larger than the initial equilibrium pressure; otherwise the system becomes unstable. In the second-order theory, we take the initial value of the bulk pressure to be the same as in the first-order theory. Using this initial condition allows for a direct comparison, since both theories start from the same initial values. Moreover, on physical grounds, if τ_0 is to be interpreted as the onset of hydrodynamic behavior (thermalization time), then the Reynolds number at τ_0 should be stationary, i.e., it should neither grow nor decrease; this implies that the initial value for the bulk pressure should be close to that given by the first-order approach [62].

We can see in Fig. 4.12 that the flow velocity and expansion rate are fairly well reproduced for the second-order theory while the results for the first-order theory show large numerical artifacts already at a few fm distance from the center. This is correlated with the coarse-graining, since the results

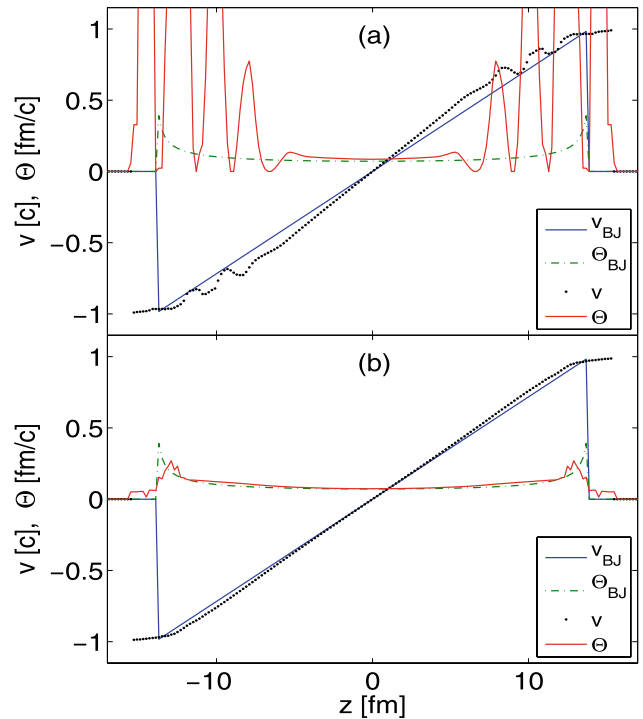


Fig. 4.12 The exact velocity v_{BJ} (full line) and expansion rate Θ_{BJ} (dash dotted line), compared to the numerically calculated velocity v (dotted line) and expansion rate Θ (full line), for a dissipative fluid with $\zeta/s = 0.2$ after $\Delta t = 8 \text{ fm}/c$ evolution. **a** First-order theory; **b** second-order theory with $\tau_\Pi = 1 \text{ fm}/c$ constant relaxation time. In both cases the initial value for the bulk pressure is given by the Navier–Stokes value

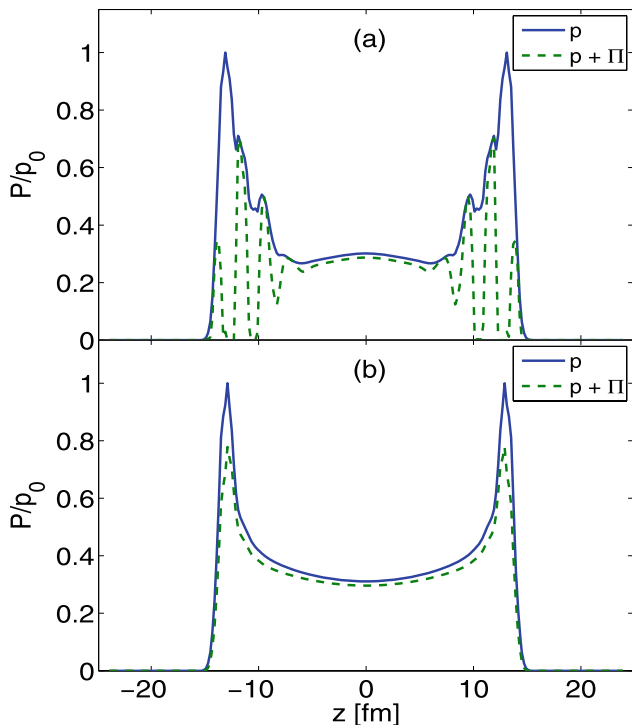


Fig. 4.13 The effective pressure normalized by the initial pressure. **a** First-order theory; **b** second-order theory. The parameters are the same as in Fig. 4.12

improve on finer grids.⁴ We can also observe the large prediffusion into vacuum due to reduced antidiffusion similarly to the Riemann wave discussed above. The fluctuations in the velocity are also visible in the expansion rate and in the pressure shown in Fig. 4.13.

We have also tested how well the algorithm solves the relaxation equation for the bulk pressure. This is important to know, since the SHASTA was specially designed to solve conservation equations. We have plotted the evolution of the bulk pressure in the central cell, which has a velocity $v \approx 0$, next to the results of a standard fourth-order Runge–Kutta solver. The comparison in case of first-order theory is given in Fig. 4.14a. Here $\Pi_{1(\text{RK})}$, indicated with a full line is the Runge–Kutta solver, while the result of SHASTA is Π_1 , indicated with a dashed line. The curves match reasonably well; deviations are due to the overestimate of the local expansion rate.

For second-order theories our standard choice for the initial value of the bulk pressure is given by the Navier–Stokes value; this corresponds to $\Pi_{2(\text{RK})}$ and Π_2 in Fig. 4.14b. We have also compared to the case when the system starts from

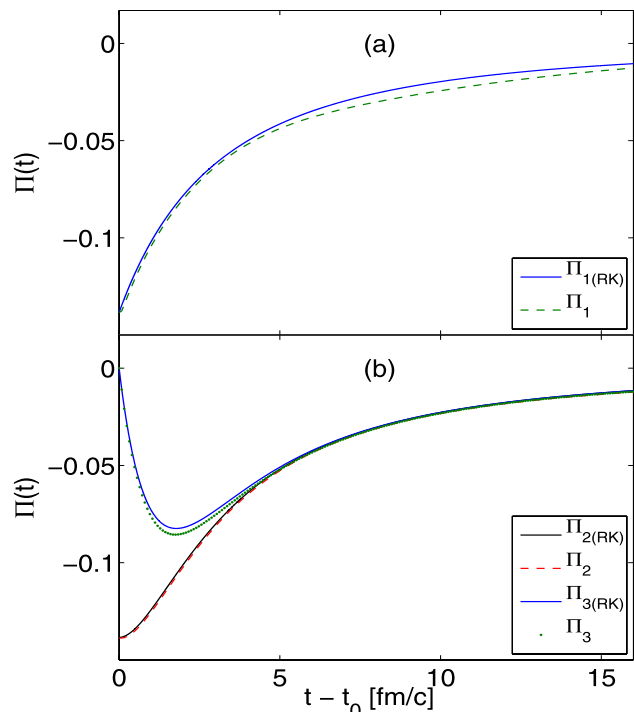


Fig. 4.14 The evolution of the bulk pressure in a central cell. **a** First-order theory; **b** second-order theory. The initial condition for the bulk pressure is given by the Navier–Stokes value for Π_1 , Π_2 , $\Pi_{1(\text{RK})}$ and $\Pi_{2(\text{RK})}$. The evolution of the initially equilibrated system are for Π_3 and $\Pi_{3(\text{RK})}$

equilibrium⁵ ($\Pi(t_0) = 0$); see the curves $\Phi_{3(\text{RK})}$ and Φ_3 . In both cases the SHASTA result is very good. There are some small deviations, however, due to the difference between the calculated and analytical expansion rates. We have checked our calculations using the exact expansion rate $\theta = 1/\tau$ and in this case not only the second-order calculations but also the first-order ones are smooth and very accurately match the Runge–Kutta results.

5 Summary and outlook

In this work we have focused on testing numerical solutions of first- and second-order theories of relativistic hydrodynamics with bulk viscosity using the SHASTA flux corrected transport algorithm. This is a rather efficient and fast algorithm for solving causal fluid transport on a fixed grid; it provides accurate solutions of ideal hydrodynamics with minimal numerical viscosity and prediffusion and can be easily adapted to multi-dimensional problems. In fact, the algorithm can also be used to solve the relaxation equations of the second-order approach simultaneously with the

⁴In view of forthcoming applications to 3-dimensional problems we only consider grids with at most a few hundred grid cells.

⁵Note that, as mentioned above, for such a type of initial conditions the dissipative corrections initially grow very rapidly, which is not a physically plausible scenario [62].

conservation equations without resorting to other numerical schemes, which may reduce the computational time and complicate the problem and its implementation further.

The first-order theory of viscous hydrodynamics provides the proper description of long-wavelength, low-frequency density waves in a fluid. The second-order theory introduces relaxation equations for the dissipative fluxes thereby maintaining causality. Its solutions converge to those of the first-order theory over time scales larger than the relaxation times. It has been argued that these relaxation times might be on the order of the microscopic time scales in the problem and that the second-order theory is therefore no better approximation to the dynamics than the first-order approach.

Our numerical solutions with the SHASTA algorithm, however, indicate that the accuracy and stability of the solutions of the second-order theory is significantly better than in the first-order theory, even if the calculated local expansion rate is smoothed over a few fluid cells: the solution of the Riemann wave with viscosity in the first-order approach produces oscillations which are absent from the second-order theory. This observation holds for virtually any amount of dissipation. Also, the numerical problems encountered in the first-order approach get milder if the speed of sound is smaller (which reduces the acceleration of the flow) but worse if the equation of state is stiff.

These observations are valid in the 2- or 3-dimensional cases [63]; therefore, in conclusion, we believe that for general purpose codes the second-order theory is not only more general, but also more stable and reliable, even numerically. Although using the second-order theory it is computationally more intensive since the dissipative quantities have to be propagated in time, its implementation into some existing numerical codes which solve hyperbolic partial differential equations in conservation form, does not require more effort than adding the first-order corrections.

Regardless of the difference between numerical methods, using the same initial conditions and corresponding physical quantities, all numerical results should be very closely the same. Unfortunately, in case of dissipative fluid dynamics there are only a few simple solutions where the numerical accuracy can be tested in great detail. However, taking into account that actual applications of relativistic fluid dynamics in modeling relativistic heavy-ion collisions need several other crucial approximations (introducing additional uncertainties and parameters linked to the fluid dynamical calculation, such as initial conditions and freeze-out), it is of great importance that the numerical fluid dynamical methods should be very carefully investigated, tested and documented in various situations. To our knowledge, in most publications this topic is rather forgotten and/or undisclosed. The other reliable possibility and recommendation would be to check the fluid dynamical codes against kinetic theory [64, 65], which on the other hand would also ‘validate’ transport codes in the fluid dynamical regime.

Note added: during the preparation of this manuscript we became aware of the very recent work by the Brazilian group [66, 67], on the shock propagation and stability in causal 1 + 1 dimensional dissipative hydrodynamics, using the smoothed particle hydrodynamics (SPH). This important problem was also investigated by us with the relaxation method presented in this paper, and it lead to very promising agreement with kinetic theory [68].

Acknowledgements The author thanks A. Dumitru for the guidance, discussions, careful reading and corrections. Furthermore, the author is thankful to D.H. Rischke for the original version of ideal SHASTA code and many important comments and suggestions. The author also thanks to H. Niemi for checking independently some results presented and for his clarifying comments and recommendations. Enlightening discussion on the topic with T.S. Biró, L.P. Csernai, M. Gyulassy, J.A. Maruhn and I. Mishustin are noted. Constructive comments by an anonymous referee are noted with warm feelings. We gratefully acknowledge support by the Alexander von Humboldt foundation.

Appendix A

Here we approximately extract and quantify the numerical errors and uncertainties as a function of time and viscosity. Since the exact solution for the Riemann problem with dissipation is unknown, the deviation from analytic solutions cannot be measured. However, since the second-order solutions converge to the first-order solutions at late times, we may quantify the error and deviations between the outcomes, see Fig. A.1.

Therefore, we introduce the following relative deviation (point by point) between the flow velocities of matter and measure it by the following integral:

$$d(t) = \frac{1}{N} \int_{-1}^{1.5} d\xi |v_{2\text{nd}}(\xi) - v_{1\text{st}}(\xi)|, \quad (\text{A.1})$$

where the normalization factor, $N = \int_{-1}^{1.5} d\xi |v_{2\text{nd}}(\xi)|$. Note that the first-order and second-order theories start from different initial values; hence the initial deviation. We also observe that increasing the viscosity the results start to diverge at late times, signaling the instability and large errors in the numerical solution of the first-order theory. This was apparent in all figures in Sect. 4.2.

Next we discuss and show further examples and test results using different initial conditions and antidiffusion mask coefficients. Using the purely conventional initial value for the velocity of vacuum, $v = 1$ for $z > 0$, we make sure that the fluid dynamical solution is continuous at the boundary to vacuum.

This specific test ensures that the oscillations in the first-order theory are not caused by the sharp boundary, and that the oscillations propagate outwards and not inwards from the vacuum; see Fig. A.2a. Therefore, this effect is mainly

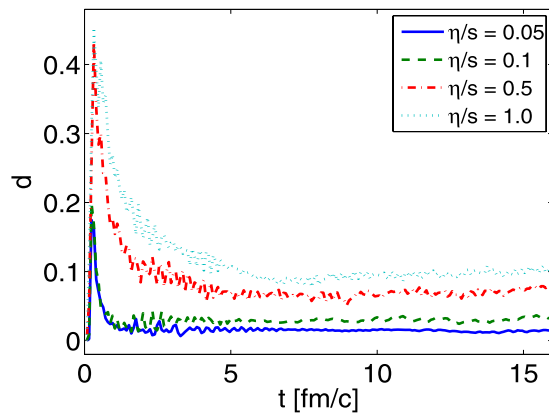


Fig. A.1 The relative difference between the first-order and second-order theory as a function of time, measured by the above integral, for values of viscosity given in the figure

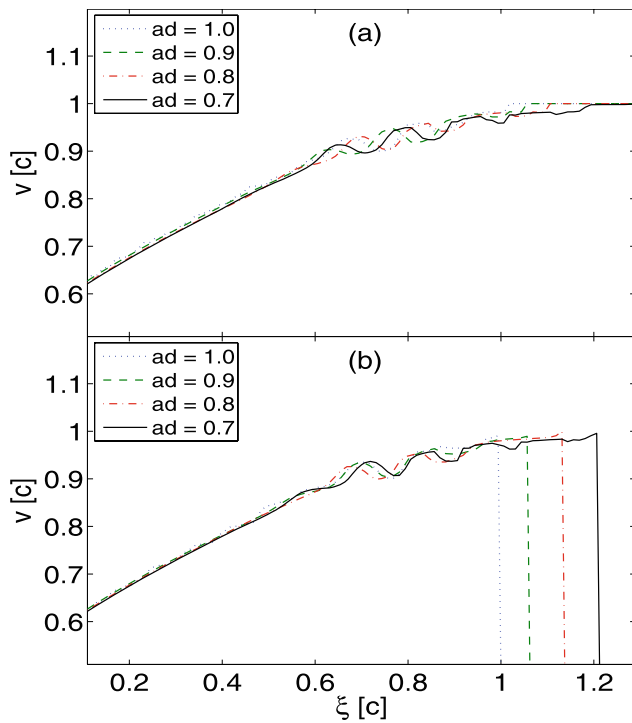


Fig. A.2 The velocity profiles as calculated numerically at $t = 16 \text{ fm}/c$ for a dissipative fluid with $\zeta/s = 0.1$ in first-order theory using different antidiffusion mask coefficients (ad) as shown on the figure. The initial condition in subplot **a** is $v = 1$, for $z > 0$, it guarantees a continuous solution at the boundary to the vacuum. In **b** we have $v = 0$ for $z > 0$

due to two things. First the higher-order derivatives of the flow velocity appear in the equations and therefore even very small fluctuations in the flow field are enhanced and couple back into the solution. The second feature is a purely numerical problem, which unfortunately affects of the numerical scheme and its accuracy, since the SHASTA algorithm

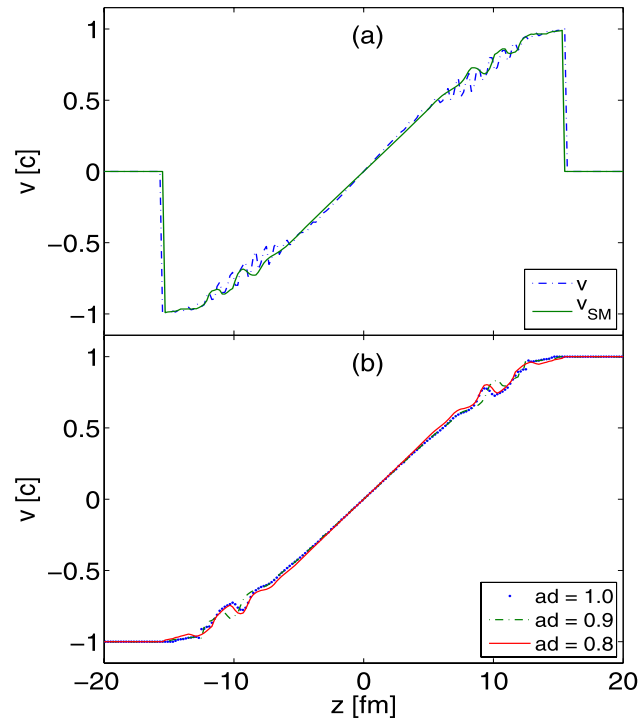


Fig. A.3 The velocity profile for a Bjorken expansion in first-order theory for $\zeta/s = 0.2$ after $\Delta t = 8 \text{ fm}/c$ evolution. On **a** the un-smoothed versus the smoothed v_{SM} velocity profile with ad = 0.8 mask coefficient. The continuous boundary condition for the velocity with various mask coefficients on **b**

was not explicitly designed to solve the relativistic Navier–Stokes equations.

We also see the effect of a further numerical artifact namely reducing the antidiffusion coefficient by 10%, 20% and 30% not only increases the entropy in the system, but it also gives as a result non-linear changes and differences in the solutions. The standard version of the algorithm uses a mask coefficient equal to 1. We can see in Figs. A.2 and A.3b that using a 20% smaller mask is reasonably close to the solution with the standard value of the mask, but, more importantly, the results become much smoother.

In Fig. A.3a we have plotted the velocity profile calculated with a 20% reduced antidiffusion for a smoothed and un-smoothed expansion rate. We can see that the smoothing affects the solution positively leading to even less prediffusion into vacuum in this particular case.

Appendix B

Here we recall the solutions for the expansion into vacuum in case of a perfect fluid, following [69]. Introducing the similarity variable, $\xi = z/t$, the partial derivatives transform as $\partial_t = -(\xi/t)(d/d\xi)$ and $\partial_z = (1/t)(d/d\xi)$. Therefore, the equation for the energy and momentum in terms of the rest

frame quantities becomes

$$(v - \xi)\gamma^2 \frac{de}{d\xi} + [v + (v - \xi)v^2\gamma^2] \frac{dP}{d\xi} + \gamma^2(e + P)[(v - \xi)(2v\gamma^2) + 1] \frac{dv}{d\xi} = 0, \quad (\text{B.1})$$

$$(v - \xi)v\gamma^2 \frac{de}{d\xi} + [1 + (v - \xi)v\gamma^2] \frac{dP}{d\xi} + \gamma^2(e + P)[(v - \xi)(1 + 2v^2\gamma^2) + v] \frac{dv}{d\xi} = 0. \quad (\text{B.2})$$

Using the standard EOS, $P = c_s^2 e$, the vanishing determinant of the above system of equations leads to the expression for the characteristic variable, $\xi = \frac{v \pm c_s}{1 \pm v c_s}$. The correct solutions imply (4.1); hence we are lead to the following trivial equation:

$$\frac{de}{e} = -\frac{(1 + c_s^2)}{c_s} \frac{dv}{(1 - v^2)}, \quad (\text{B.3})$$

which with the corresponding initial conditions given in Sect. 4.1 leads to the results presented before.

Viscosity is introduced by $P = c_s^2 e + \Pi$, where the expansion rate is

$$\partial_\mu u^\mu = (1 - v\xi) \frac{\gamma^3}{t} \frac{dv}{d\xi}. \quad (\text{B.4})$$

Using the expression for the dissipative pressure in first-order theory, $dP/d\xi$, leads to terms containing, $d^2 v/d\xi^2$, $(dv/d\xi)^2$, $d\xi/d\xi$ and $dt^{-1}/d\xi = -t/\xi$; therefore, even in this simple case the exact solution is unknown. In second-order theory, the relaxation equation is

$$(v - \xi)\gamma \frac{d\Pi}{d\xi} - \frac{\zeta}{\tau_\Pi} (1 - v\xi)\gamma^3 \frac{dv}{d\xi} = -\frac{t}{\tau_\Pi} \Pi, \quad (\text{B.5})$$

while the derivative of the pressure reduces to $dP/d\xi = c_s^2 de/d\xi + d\Pi/d\xi$. In conclusion, we see that for dissipative fluids the equations depend explicitly on the time in the local rest frame, and the similarity of the flow is broken.

References

1. RHIC Scientists Serve Up “Perfect” Liquid. http://www.bnl.gov/bnlweb/pubaf/pr/PR_display.asp?prID=05-38
2. C. Eckart, Phys. Rev. **58**, 919 (1940)
3. L.D. Landau, E.M. Lifshitz, *Fluid Dynamics*, 2nd edn. (Butterworth-Heinemann, London, 1987)
4. W. Israel, Ann. Phys. **100**, 310 (1976)
5. J.M. Stewart, Proc. R. Soc. A **357**, 57 (1977)
6. W. Israel, J.M. Stewart, Ann. Phys. **118**, 341 (1979)
7. A. Muronga, Phys. Rev. Lett. **88**, 062302 (2002) (Erratum-ibid. **89**, 159901 (2002))
8. A. Muronga, Phys. Rev. C **69**, 034903 (2004)
9. A. Muronga, D.H. Rischke, <arXiv:nucl-th/0407114>
10. D.A. Teaney, J. Phys. G **30**, S1247 (2004). <arXiv:nucl-th/0403053>
11. U.W. Heinz, H. Song, A.K. Chaudhuri, Phys. Rev. C **73**, 034904 (2006)
12. R. Baier, P. Romatschke, U.A. Wiedemann, Phys. Rev. C **73**, 064903 (2006)
13. A.K. Chaudhuri, Phys. Rev. C **74**, 044904 (2006)
14. R. Baier, P. Romatschke, Eur. Phys. J. C **51**, 677 (2007)
15. P. Romatschke, U. Romatschke, Phys. Rev. Lett. **99**, 172301 (2007)
16. H. Song, U.W. Heinz, Phys. Rev. C **77**, 064901 (2008). <arXiv:0712.3715> [nucl-th]
17. H. Song, U.W. Heinz, Phys. Rev. C **78**, 024902 (2008). <arXiv:0805.1756> [nucl-th]
18. K. Dusling, D. Teaney, Phys. Rev. C **77**, 034905 (2008)
19. P. Kovtun, D.T. Son, A.O. Starinets, Phys. Rev. Lett. **94**, 111601 (2005). <arXiv:hep-th/0405231>
20. T. Hirano, M. Gyulassy, Nucl. Phys. A **769**, 71 (2006). <arXiv:nucl-th/0506049>
21. L.P. Csernai, J.I. Kapusta, L.D. McLerran, Phys. Rev. Lett. **97**, 152303 (2006). <arXiv:nucl-th/0604032>
22. P. Arnold, C. Dogan, G.D. Moore, Phys. Rev. D **74**, 085021 (2006)
23. D. Kharzeev, K. Tuchin, <arXiv:0705.4280> [hep-ph]
24. F. Karsch, D. Kharzeev, K. Tuchin, Phys. Lett. B **663**, 217 (2008)
25. H.B. Meyer, Phys. Rev. Lett. **100**, 162001 (2008)
26. G. Torrieri, B. Tomasik, I. Mishustin, Phys. Rev. C **77**, 034903 (2008). <arXiv:0707.4405> [nucl-th]
27. A. Muronga, Phys. Rev. C **76**, 014909 (2007)
28. I.S. Liu, I. Müller, T. Rugerri, Ann. Phys. **169**, 191 (1986)
29. R. Geroch, L. Lindblom, Phys. Rev. D **41**, 1855 (1990)
30. R. Geroch, J. Math. Phys. **36**(8), 4226 (1995)
31. J. Gariel, G. Le Denmat, Phys. Rev. D **50**, 2560 (1994)
32. T. Koide, G.S. Denicol, P. Mota, T. Kodama, Phys. Rev. C **75**, 034909 (2007). <arXiv:hep-ph/0609117>
33. G.S. Denicol, T. Kodama, T. Koide, P. Mota, Braz. J. Phys. **37**, 1047 (2007)
34. P. Van, T.S. Biro, Eur. Phys. J. ST **155**, 201 (2008). <arXiv:0704.2039> [nucl-th]
35. T.S. Biro, E. Molnar, P. Van, Phys. Rev. C **78**, 014909 (2008). <arXiv:0805.1061> [nucl-th]
36. P. Van, <arXiv:0811.0257> [nucl-th]
37. T. Osada, G. Wilk, <arXiv:0810.3089> [hep-ph]
38. T. Osada, G. Wilk, <arXiv:0810.5192> [nucl-th]
39. W.A. Hiscock, L. Lindblom, Ann. Phys. **151**, 466 (1983)
40. W.A. Hiscock, L. Lindblom, Phys. Rev. D **31**, 725 (1985)
41. W.A. Hiscock, Phys. Rev. D **33**, 1527 (1986)
42. W.A. Hiscock, L. Lindblom, Phys. Rev. D **35**, 3723 (1987)
43. I. Müller, Z. Phys. **198**, 329 (1967)
44. C. Truesdell, Proc. R. Soc. A **226**, 59 (1954)
45. W. Israel, J. Math. Phys. **4**(9), 1163 (1963)
46. W. Zimdahl, Phys. Rev. D **53**, 5483 (1996)
47. R. Maartens, <arXiv:astro-ph/960911>
48. R. Maartens, V. Méndez, Phys. Rev. D **55**, 1937 (1997)
49. K. Paech, S. Pratt, Phys. Rev. C **74**, 014901 (2006)
50. J.P. Boris, D.L. Book, J. Comput. Phys. **11**, 38 (1973)
51. J.P. Boris, D.L. Book, J. Comput. Phys. **135**, 172 (1997)
52. V. Schneider et al., J. Comput. Phys. **105**, 92 (1993)
53. D.H. Rischke, S. Bernard, J.A. Maruhn, Nucl. Phys. A **595**, 346 (1995)
54. D.J. Dean et al., Phys. Rev. E **49**, 1726 (1994)
55. G. Tóth, D. Odstrcil, J. Comput. Phys. **128**, 82 (1996)
56. J. Liu, E.S. Oran, C.R. Kaplan, J. Comput. Phys. **208**, 416 (2005)
57. D.L. Book, C. Li, G. Patnaik, F.F. Grinstein, J. Sci. Comput. **6**, 323 (1991)
58. J.D. Anderson Jr., *Computational Fluid Dynamics* (McGraw-Hill, New York, 1995)

59. L. Mornas, U. Ornik, Nucl. Phys. A **587**, 828 (1995). [arXiv:nucl-th/9412012](https://arxiv.org/abs/nucl-th/9412012)
60. G. Torrieri, I. Mishustin, Phys. Rev. C **78**, 021901 (2008). [arXiv:0805.0442](https://arxiv.org/abs/0805.0442) [hep-ph]
61. J.D. Bjorken, Phys. Rev. D **27**, 140 (1983)
62. A. Dumitru, E. Molnar, Y. Nara, Phys. Rev. C **76**, 024910 (2007). [arXiv:0706.2203](https://arxiv.org/abs/0706.2203) [nucl-th]
63. E. Molnar et al. (2009, to be published)
64. D. Molnar, P. Huovinen, J. Phys. G **35**, 104125 (2008). [arXiv:0806.1367](https://arxiv.org/abs/0806.1367) [nucl-th]
65. P. Huovinen, D. Molnar, Phys. Rev. C **79**, 014906 (2009). [arXiv:0808.0953](https://arxiv.org/abs/0808.0953) [nucl-th]
66. G.S. Denicol, T. Kodama, T. Koide, Ph. Mota, Phys. Rev. C **78**, 034901 (2008). [arXiv:0805.1719](https://arxiv.org/abs/0805.1719) [hep-ph]
67. G.S. Denicol, T. Kodama, T. Koide, Ph. Mota, [arXiv:0808.3170](https://arxiv.org/abs/0808.3170) [hep-ph]
68. J. Bouras et al., Relativistic shock waves in viscous gluon matter (2009). [arXiv:0902.1927](https://arxiv.org/abs/0902.1927) [hep-ph]
69. J. Centrella, J.R. Wilson, Astrophys. J. Suppl. **54**, 229 (1984)